Highly Linear Phase-Canceling Self-Injection-Locked Ultrasonic Radar for Non-Contact Monitoring of Respiration and Heartbeat

Shiang-Hwua Yu, *Member, IEEE*, and Tzyy-Sheng Horng, *Fellow, IEEE*

***Abstract*—A novel phase-canceling demodulation scheme to improve the linearity of a self-injection-locked (SIL) ultrasonic radar is proposed with the goal of solving the null detection problem and accurately sensing large displacements of a moving target. A proportional-integral (PI) controller regulates the phase of the injection signal and cancels the Doppler phase shift by tuning a delay in the received echo signal, and this tunable delay serves as the radar output, which is linearly proportional to the displacement of the target. Without assuming weak injection, the frequency and phase equations for an SIL oscillator are derived, supporting the construction of a plant model and the design of a PI controller. Also, a new ultrasonic radar equation is presented for estimating the radar detection range. The SIL radar with phase regulation is operated in its anti-phase injection mode for better performance. The proposed design is implemented on an FPGA to make a 40 kHz continuous-wave ultrasonic radar. The maximum detectable peak-to-peak motion is up to 120 mm (approximately 14 wavelengths of displacement), with a total harmonic distortion as low as 2.3% for the detection of 1 Hz harmonic motion. The radar is used to detect the human chest movement for non-contact monitoring of the respiratory rate and heart rate. Due to the high linearity and sensitivity, the radar is capable of faithfully detecting the relatively large involuntary body movements and lung movements while still preserving the weak heartbeat rhythm buried in them, with the average error of measured heart rates less than 1 BPM.**

***Index Terms*—Anti-phase injection mode, doppler radar, motion detection, phase regulation, self-injection-locked oscillator, vital sign detection.**

I. Introduction

SINCE more than four decades ago, when continuous-wave Doppler radars found use to monitor respiration and heartbeats [1]–[4], the development of more accurate and reliable Doppler radars for detecting vital signals has continued to stimulate interest [5]–[11]. Significant progress has been made in improving the sensitivity of these radars using the *injection locking* technique [12]–[15]. The resulting self-injection-locked (SIL) radar features low circuit complexity, good noise immunity, and high sensitivity [9]–[11]. The core of an SIL radar is an SIL oscillator [15], which generates a carrier signal for a transmitter and is injected with the returned echo signal that is sensed by a receiver. The oscillator operates in SIL mode, in which its oscillation frequency and amplitude vary with the Doppler phase shift induced by the motion of the target. Therefore, the motion can be extracted from the oscillation signal.

In the authors' opinion, all of the difficulties that are associated with the Doppler radar or SIL radar may be reduced to a single problem: the intrinsic trigonometric nonlinearity makes detection of a large movement without distortion very difficult. As the target moves through a distance of more than a quarter wavelength, the radar sees the Doppler phase shift's passing through null points [10], [16], [18] (for both the Doppler and SIL radars) or a range of unstable points [15] (for the SIL radar only) and yields a seriously distorted output. A simple and effective method for preventing distortion is to limit the target displacement to only a small fraction of a wavelength and carefully adjust the initial position of the target or simply add a tunable phase lag to the received signal to ensure that the detection point is optimal [16]. Selecting the operating frequency for the best performance is to compromise between linearity and sensitivity. A lower operating frequency allows the radar to have a wider linear sensing range at the cost of lower sensitivity, because the phase shift that is induced by a particular displacement will be smaller if the wavelength is longer.

Many attempts have been made to solve the problem of nonlinearity of the radar; most notable among them are the *arctangent demodulation* method [17]–[22] and the *phase tracking demodulation* method [2]–[4], [7]. The arctangent demodulation method is based on the quadrature phase detection technique, which involves applying arctangent demodulation to the ratio of the quadrature outputs and then performing phase unwrapping to extract the Doppler phase shift. Theoretically, the null point problem is completely solved in this way; in practice, however, due to circuit dc offset and quadrature channel imbalance, a certain degree of distortion occurs at the radar output, especially when either of the quadrature outputs is close to the null point. The precision of this popular method depends strongly on how

Manuscript received August 17, 2019; revised November 14, 2019; accepted December 4, 2019. Date of publication December 9, 2019; date of current version February 4, 2020. This work was supported by the Ministry of Science and Technology, Taiwan, under Grant MOST 108-2221-E-110-007-MY2. The paper was recommended by Associate Editor S. O'Driscoll. *(Corresponding author: Shiang-Hwua Yu.)*

The authors are with the Department of Electrical Engineering, National Sun Yat-sen University, Kaohsiung 804, Taiwan (e-mail: shaun@mail.ee.nsysu.edu.tw; jason@ee.nsysu.edu.tw).

Digital Object Identifier 10.1109/TBCAS.2019.2958598

effectively the circuit imperfections can be corrected [18] and the effectiveness of the phase unwrapping algorithm [21], [22]. The phase tracking demodulation method, first developed by Dr. Northrop and his colleague Nilakhe in 1976 [2], has received much less attention than the arctangent demodulation method. The phase tracking demodulation method employs a phase locked loop (PLL) to synchronize the transmitted and received signals by tuning the frequency of the transmitter, thereby maintaining a fixed number of wavelengths of propagation between the radar and the moving target. Consequently, the frequency variation, which is inversely proportional to the displacement of the target, can be extracted from the input of the voltage-controlled oscillator in the feedback loop. The phase tracking method is less prone than the arctangent demodulation method, to circuit imperfections and thus has better linearity. A small dc offset in the phase detector of the PLL does not affect the detection of motion, and the precision of detection can be maintained as long as the transmitted and received signals remain synchronized. The major weakness of the phase tracking demodulation method is that its detectable range of motion is seldom greater than two wavelengths, because it is strictly restricted by the frequency tuning range of the PLL and the transceiver bandwidth.

The work intends to apply the SIL mechanism to an ultrasonic radar for the first time. Moreover, it improves over the drawbacks of the above-mentioned methods by presenting a novel *phase-canceling* technique that effectively increases the linear sensing range of an SIL radar while maintaining good immunity to noise and circuit imperfections. The proposed phase-canceling design exploits the idea of phase regulation via feedback, similar to the PLL in [2]–[4], [7]. The phase-canceling SIL radar cancels the Doppler phase shift by adding a variable delay in the received echo signal, making the SIL radar see no phase change in the injected echo signal. This situation is akin to electronically moving the radar in synchrony with the moving target. Consequently, the motion of the target can be directly extracted from the tunable delay d that cancels the Doppler phase shift. Experiments indicate that the resulting SIL radar has high linearity over a very wide sensing range, and it can sense a harmonic motion over 14 wavelengths with a total harmonic distortion of only 2.3%.

II. Nonlinearity of an SIL Radar

For convenience, some important facts concerning the self-injection-locked (SIL) radar are recapitulated here, with particular emphasis on its nonlinear characteristics.

Fig. 1 shows a block diagram of an SIL microwave radar, which consists of a self-sustained oscillator, amplifiers, microwave antennas, and a demodulator. The radar signal u, generated by the oscillator, is emitted via a transmitter. At the heart of radar detection is the injection of the scaled and delayed version of the oscillation signal. The transmitted microwaves are reflected by a moving target, sensed by the receiver, and then injected back into the oscillator. The phase of the injection signal affects the oscillation frequency and amplitude of the oscillator. Based on the assumption that the frequency shift is small, the

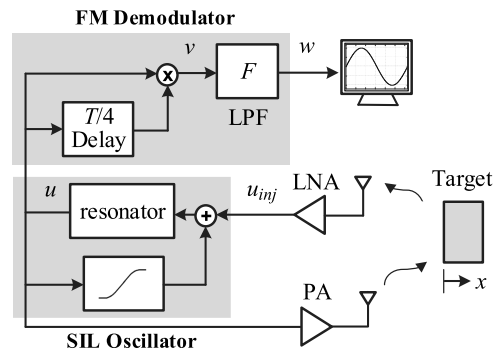

Fig. 1. Conventional direct demodulation of an SIL microwave radar.

phase difference θ between u and u_{inj} is roughly determined by the total elapsed time D as follows.

$$\theta(t) \approx \omega_n D(t), \quad D(t) = \frac{2}{c}\left[R_0 + x(t)\right], \tag{1}$$

where ω_n is the free-running frequency of the oscillator without any injection; c is the propagation speed; R_0 is the initial distance of the target from the radar, and x is the target displacement. According to *Adler's equation* [9], [12]–[14], the instantaneous oscillation frequency ω is approximately related to the phase θ by

$$\omega(t) - \omega_n \approx -\frac{\omega_n}{2Q}\frac{B}{A}\sin\left[\theta(t)\right], \tag{2}$$

where Q is the quality factor of the resonator in Fig. 1. B is the amplitude of the sinusoidal injected signal u_{inj}, and A the amplitude of the oscillation signal u. Appendix A provides another way to derive Eq. (2), without the presumption of weak injection that is commonly made in the literature [12], [14]. As indicated in (1) and (2), the target displacement x causes a change in the phase θ, which in turn results in modulation of the oscillation frequency ω. The sine function on the right hand side of (2) characterizes the major nonlinearity in the extraction of x from the frequency shift $\Delta\omega = \omega - \omega_n$ by frequency demodulation.

Note that the frequency shift is a periodic function of the distance. A simple approach to mitigating the nonlinearity is to place the target at an appropriate distance so that θ departs only slightly from an integer multiple of 2π. Hence, the frequency shift $\Delta\omega$ is almost linearly proportional to the Doppler phase shift $\Delta\theta$ and thus to the displacement x as well.

$$\Delta\omega(t) \approx -\frac{\omega_n}{2Q}\frac{B}{A}\sin\left[\Delta\theta(t)\right] \approx -\frac{\omega_n}{2Q}\frac{B}{A}\Delta\theta(t), \tag{3}$$

where

$$\Delta\theta(t) \approx \frac{2\omega_n}{c}x(t) = \frac{4\pi}{\lambda}x(t). \tag{4}$$

Since a null point exists at every quarter wavelength $\lambda/4$ of distance, this approach imposes a serious restriction on the target's initial position and allowable displacement.

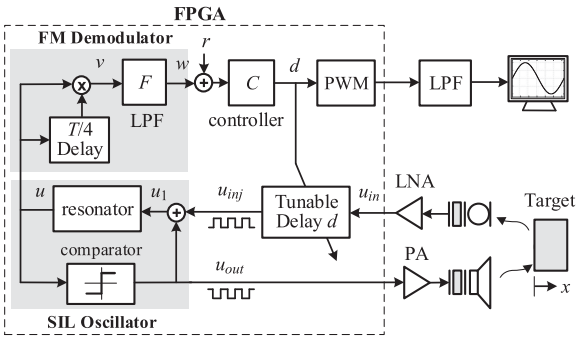

Fig. 2. Proposed feedback demodulation of an SIL ultrasonic radar.

III. SIL Radar With Feedback Demodulation

Fig. 2 presents a feedback design for an SIL ultrasonic radar to tame the nonlinearity problem. Sharp-eyed readers will notice that it is basically a conventional SIL radar added with a feedback tunable delay line. The design is based on the previously made observation: the nonlinearity can be eliminated by constraining θ to the close vicinity of the desired operating point. To this end, a dynamically tuned delay line is added to cancel the variations of the round-trip delay caused by the target motion by regulating the total phase θ to a desired constant value. As a result of the cancellation of the Doppler phase shift, the tuned delay d can serve as the radar output, for its properly scaled waveform automatically copies the trajectory of the moving target with great precision. Phase regulation ensures $\theta(t) \approx \omega_n[D(t) + d(t)] =$ constant; substituting D in (1) into it yields the estimated trajectory $\hat{x}$ as below.

$$\hat{x}(t) = -0.5c[d(t) - a]. \tag{5}$$

The estimated trajectory $\hat{x}$ is obtained by firstly removing the dc component, a, from the tunable delay signal d, and then scaling it by a factor $-0.5c$.

The proposed phase regulator C adjusts the tunable delay d by monitoring the frequency shift $\Delta\omega = \omega - \omega_n$ rather than the phase θ. It works well because the frequency shift is approximately linearly proportional to a small phase variation around the desired set-point $\theta = 0$ or $\theta = \pi$, as implied by (2). The frequency shift is detected by a phase-shift discriminator [23]. The delay time in the $T/4$ delay block in Fig. 2 is a quarter of the free-running oscillation period, namely $T/4 = \pi/(2\omega_n)$.

For ease of digital implementation, a comparator in Fig. 2 is used in place of a saturated amplifier, which is commonly used in a SIL oscillator to sustain the oscillation of a resonator. The resulting oscillator is commonly known as a relay-feedback oscillator [24], [25]. Another modification is that both the driving signal u_{out} and the injected signal u_{inj} are square waves to facilitate implementation on an FPGA without any on-chip analog-to-digital converters.

This design raises the question of how best to design a phase regulator C. Without loss of generality, the following analysis considers the normalized case in which the demodulating filter F has a unity dc gain; the resonator is a high-Q second-order bandpass filter with unity peak gain; the amplitude of the driving square wave u_{out} is 1, and the amplitude of the injected square wave u_{inj} is A_{inj}. Thus, the injected square wave contains fundamental sinusoid with amplitude $B = 4A_{inj}/\pi$, which will be substituted into (2) for deriving the plant model.

A. Modelling

Before a controller C is designed, a plant model–an approximate transfer function from the tunable delay d (control signal) to the demodulator output w (feedback signal)–is required. Appendix B derives the following small-signal model.

$$P(s) = g(\theta; A_{inj})e^{-s\frac{T}{8}}F(s), \tag{6}$$

where

$$g(\theta; A_{inj}) = \frac{2A_{inj}\cos(\theta)[1 + A_{inj}\cos(\theta)]\omega_n}{\pi Q}. \tag{7}$$

The plant model includes the transfer function $F(s)$ of the demodulating filter, a small delay of one eighth of the free-running oscillation period, and a gain g that depends on the injected square-wave amplitude A_{inj}, the resonator's quality factor Q and resonance frequency ω_n, and the phase θ.

Due to its nonlinearity, the plant gain g varies with the operating point θ. Consider two candidate points $\theta = 0$ and $\theta = \pi$ at which the plant has better linearity with a flat gain. In-phase injection occurs when $\theta = 0$ (u_{inj} and u_{out} are in-phase), resulting in a pronounced maximum in the oscillation amplitude, and the plant gain g is positive in this case. Anti-phase injection occurs when $\theta = \pi$(u_{inj} and u_{out} are out-of-phase), yielding a minimum in the oscillation amplitude and a negative plant gain. The controller regulates the phase θ according to the set-point r. The tricky part is that according to (2), both the operating points $\theta = 0$ and $\theta = \pi$ correspond to the same set-point $r = 0$ (a zero frequency shift $\Delta\omega = 0$). The actual operating point is determined by the sign of the controller gain. For example, given a set-point $r = 0$ and a positive-gain controller, the phase control system, if stable, will be stabilized in a negative-feedback manner at $\theta = \pi$, at which the plant has a negative gain. Changing the sign of the controller gain, we can change the operating point. We now need to ask which is the better operating point– $\theta = 0$ or $\theta = \pi$? More studies are required to answer it.

B. Desired Operating Point

The nonlinearity results in a plant gain that changes with the operating point. One way of thinking about choosing the best possible operating point is to make the plant as linear as possible by setting an operating point near which the plant gain is almost constant.

Close inspection of (6) reveals that if the injection level $A_{inj} = 0.5$ is chosen, then the plant gain g exhibits the following maximal-flatness property at $\theta = \pi$:

$$\frac{dg}{d\theta} = \frac{d^2g}{d\theta^2} = \frac{d^3g}{d\theta^3} = 0. \tag{8}$$

Fig. 3 plots the plant gain in (7) with $A_{inj} = 0.5$. It is indeed almost constant near the point $\theta = \pi$, which means that the plant

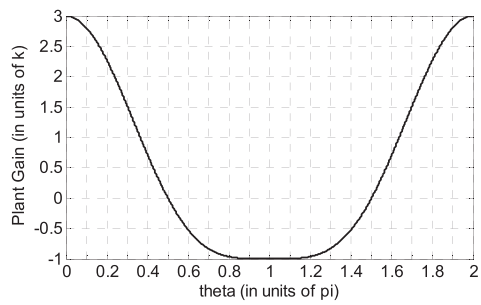

Fig. 3. Graph of plant gain g versus operating point θ, which is maximally flat at $\theta = \pi$ with the injection amplitude $A_{inj} = 0.5$. The plant gain is shown in units of k defined in (10).

exhibits fairly good linearity even under a large phase swing. Given $\theta = \pi$ and $A_{inj} = 0.5$, the plant model becomes

$$P(s) = -ke^{-\frac{T}{8}s}F(s), \tag{9}$$

where the gain k equals the resonator bandwidth (in Hz):

$$k = f_n/Q = 1/(QT), \tag{10}$$

with $f_n = \omega_n/(2\pi)$. The maximum-flatness property at the operating point $\theta = \pi$ justifies the subsequent use of a constant-gain linear model in the controller design.

C. Controller Design

The control problem considered here is a typical set-point regulation and disturbance rejection problem. The Doppler phase shift induced by the motion of the target is regarded as the disturbance. The controller aims to cancel the phase shift and regulate the phase to the desired operating point $\theta = \pi$. A proportional-integral (PI) controller is designed by the following procedure.

DESIGN PROCEDURE

STEP 1: Determine the cutoff frequency ω_c of the demodulating filter $F(s)$ and the plant gain k in (10).

STEP 2: The PI controller is given by

$$C(s) = \frac{k_I}{s} + k_p, \tag{11}$$

where

$$k_I = \frac{\omega_{BW}}{k}, \quad k_p = \frac{k_I}{\omega_c}. \tag{12}$$

STEP 3: Given the desired stability margin, maximize the parameter ω_{BW} in (12) under the constraint that the resulting control loop has sufficient gain and phase margins.

The controller is designed in a manner similar to [26], [27], by first approximating the high-order-plus-delay plant model (9) by a simpler first-order model,

$$\hat{P}(s) = -k\omega_c/(s + \omega_c). \tag{13}$$

The above first-order model approximates the original model (9) well at low frequencies in that it preserves the original dc gain and cutoff frequency. Then, the PI controller is designed with its gains given in (12), with the aim of canceling the dynamics of the first-order plant, yielding the following open-loop transfer function.

$$C(s)\hat{P}(s) = \frac{-\omega_{BW}}{s}. \tag{14}$$

The parameter ω_{BW} can be interpreted as the desired control bandwidth since it is the frequency at which the loop gain drops to unity in (14). The great advantage of this design approach is that it cuts the number of design parameters down to only one, leaving only ω_{BW} to be specified in the design. Generally, a higher control bandwidth ω_{BW} results in better disturbance rejection but a lower stability margin. Therefore, the choice of ω_{BW} is a compromise between performance and stability.

D. Disturbance Rejection Capability

A good metric of the controller's disturbance rejection capability is the maximum allowable speed of a moving target that can still be detected by the radar. The controller should cancel phase variation and regulate the phase to the desired point $\theta = \pi$. However, owing to its limited bandwidth, the controller may not get up to speed and has a phase error $e = \theta - \pi$ if the target moves too fast. Even worse is when the absolute phase error $|e|$ exceeds 0.5π, the plant gain will change sign as depicted in Fig. 3, and the system will become unstable and lose control. It is plausible to presume a region of stability $\theta \in (0.5\pi, 1.5\pi)$ for this control system.

It is necessary to know how the maximum detectable speed $v_{\max}$ is affected by the design parameter ω_{BW}. The difficulty with estimating $v_{\max}$ arises from the nonlinearity of the plant; the plant gain drops gradually to zero as the operating point deviates from the desired operating point $\theta = \pi$. To simplify the matter, we round off the plant gain in Fig. 3 to the nearer of $-k$ and 0, yielding a simplified model with a constant gain $-k$ in $0.6\pi \le \theta \le 1.4\pi$ beyond which the gain drops to zero. This simplified model with a reduced range of operation is used to estimate the maximum detectable speed of the target, and in this case the maximum allowed phase error is $|e| \le 0.4\pi$.

The maximum detectable speed is estimated as follows. Suppose that the system is initially at the desired operating point $\theta = \pi$, and that the target begins to move away at a constant speed v. As the target moves away, the round-trip delay increases with the ramp increment $\Delta D(t) = 2vt/c$, which can be expressed in its Laplace transform as

$$\Delta D(s) = 2v/(cs^2). \tag{15}$$

The block diagram in Fig. 4 summarizes the model that is derived in Appendix B. According to the block diagram, the phase error e, which is caused by ΔD, can be expressed as

$$e(s) = \frac{\Delta D(s)\omega_n}{1 - PC} = \frac{\Delta D(s)\omega_n}{1 - k_pP - k_IP/s}. \tag{16}$$

Substituting (15) into (16) and using the final value theorem [28, p. 584] yields the steady-state phase error

$$\lim_{t\to\infty} e(t) = \lim_{s\to 0} s\frac{[2v/(cs^2)]\omega_n}{1 - k_pP - k_IP/s} = \frac{2v\omega_n}{c\omega_{BW}}. \tag{17}$$

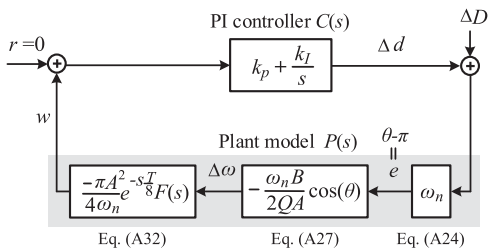

Fig. 4. Block diagram of the phase control system. See Appendix B for the detailed derivation for each block.

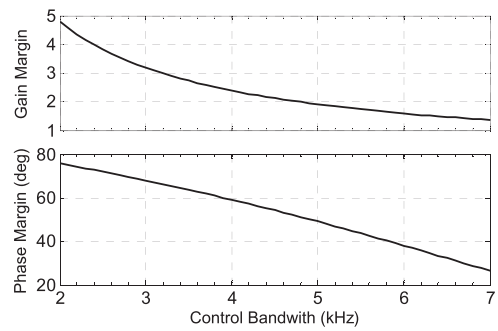

Fig. 5. Gain and phase margins versus control bandwidth.

The last equality in (17) arises from the fact that $P(0) = -k$ and $k_I = \omega_{BW}/k$. Finally, bounding the absolute steady-state phase error by 0.4π (the maximum allowable phase deviation for the simplified quantized-gain model to maintain its feedback stability) yields an upper limit for the speed of the moving target.

$$v_{\max} = \frac{\pi\omega_{BW}}{5\omega_n} c \text{ m/s}. \tag{18}$$

The maximum detectable speed $v_{\max}$ depends on the propagation speed c, the oscillator's free-running frequency ω_n, as well as the control bandwidth ω_{BW}. Among these factors, ω_{BW} is the only one that is yet to be determined. As expected, with sufficient stability, a higher ω_{BW} corresponds to better disturbance rejection by the controller and a greater ability to detect a fast target.

IV. Design and Simulation

The method presented in the preceding section is used to design an SIL ultrasonic radar, with the aim of testing the design by simulation and seeing how closely the results thereof meet the theoretical expectation.

A. Design Example: Ultrasonic Radar

Given a pair of 40 kHz ultrasonic transducers (a transmitter and a receiver), a relay-feedback oscillator, made of a resonator with a feedback connection to a comparator, is designed to have a free-running oscillation frequency of 40 kHz. The resonator is a high-Q second-order bandpass filter, with its quality factor and undamped natural frequency set as follows.

$$Q = 25,\ f_n = 4 \times 10^4 \text{ Hz}.$$

The demodulating filter F is formed by cascading two second-order lowpass Butterworth filters with cutoff frequencies of 13 kHz and 19 kHz, which together give a cutoff frequency of 11.9 kHz. Namely,

$$\begin{aligned} &\omega_c = 2\pi \times 11900 \text{ rad/s}. \\ &F = \frac{9.51\times10^{19}}{s^4+2.84\times10^5 s^3+4.04\times10^{10}s^2+2.77\times10^{15}s+9.51\times10^{19}} \end{aligned} \tag{19}$$

To obtain the maximally-flat plant gain near the desired operating point $\theta = \pi$, the amplitude of the injected square wave is set to $A_{inj} = 0.5$, yielding an associated plant model (9) with the following parameters.

$$T = 1/f_n = 2.5 \times 10^{-5},\ k = 1/(TQ) = 1600.$$

The proportional and integral gains of the PI controller are obtained from (12), leaving only parameter ω_{BW} to be adjusted. To every tentative ω_{BW} there are corresponding gain and phase margins, which can be computed by the Matlab function "margin". Fig. 5 plots the graphs of gain and phase margins against the control bandwidth $f_{BW} = \omega_{BW}/(2\pi)$ in Hz. One can choose the control bandwidth from Fig. 5 to yield the desired stability margin. For example, a phase margin of at least 60 degrees is desired; the control bandwidth 3.82 kHz may be chosen;

$$\omega_{BW} = 2\pi \times 3820 \text{ rad/s}.$$

It corresponds to a gain margin GM = 2.5 and a phase margin PM = 61 degrees. Accordingly, the gains of the PI controller are obtained:

$$k_I = 15, \quad k_p = 2 \times 10^{-4}. \tag{20}$$

The controller gain is positive, for stabilizing the radar at the desired operating point $\theta = \pi$. The maximum detectable speed of the radar can be estimated using (18), as below,

$$v_{\max} = \frac{\pi\omega_{BW}}{5\omega_n} c = \frac{\pi \times 3.82}{5 \times 40} \times 340 = 20.4 \text{ m/s}$$

B. Detection Error and Total Harmonic Distortion

The SIL ultrasonic radar with the PI controller given by (20) is simulated in Matlab. The set-point r is zero and the controller gain is positive, so the desired operating point is $\theta = \pi$. The injection amplitude is $A_{inj} = 0.5$. Since the controller output signal d (tunable delay) cannot be negative, its initial value is set to 1.2 ms, allowing a subsequent swing of ± 1.2 ms, corresponding to a maximum range of detectable displacements of about ± 20 cm, according to (1).

Suppose that an object is initially placed 30 cm away from the radar and then performs simple harmonic motion at a frequency of 10 Hz and an amplitude of 0.1 m.

$$x = 0.1\sin(2\pi \times 10t). \tag{21}$$

From (5), the estimated trajectory $\hat{x}$ can be obtained with the sound speed $c = 340$ m/s in air. Fig. 6 shows the simulated radar output $\hat{x}$ in the detection of a sinusoidal trajectory x that is given by (21). The bottom figure of Fig. 6 shows the first five milliseconds of the radar output. The radar output shows

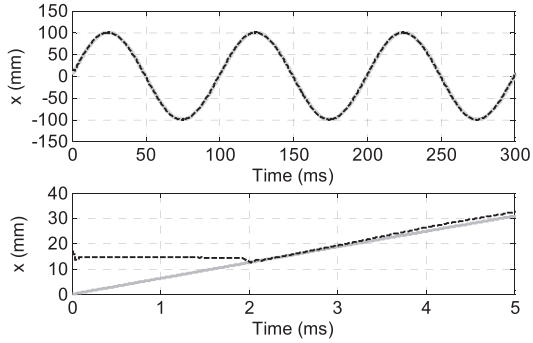

Fig. 6. Actual (gray) and measured (dashed) trajectories of the object in harmonic motion. The below is a close-up view of the above in the first five milliseconds.

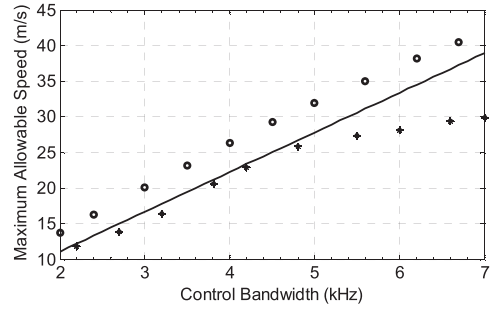

Fig. 7. Maximum allowable speed versus control bandwidth. Solid line: estimated value; circles: simulated data for 10 Hz sinusoidal target trajectories; asterisks: simulated data for 50 Hz triangular target trajectories.

about 2 ms of idle time, because that the SIL oscillator takes time to start up and transmit the ultrasound. Once the oscillator receives the echo signal whose phase is not the desired $\theta = \pi$, its frequency shift serves as a feedback signal to regulate the phase to $\theta = \pi$. The whole transient is about 2 ms before the radar really begins to track the motion of the target. The phase regulation assures that the radar performance is unaffected by the initial position of the target. As shown in Fig. 6, the radar's estimated trajectory $\hat{x}$ (dashed) matches very closely the actual trajectory x (gray). No obvious distortion is observed in the radar output, even with the total displacement of 20 cm (which is about 22.6 times the wavelength of the ultrasound in air). In contrast, a conventional SIL microwave radar will yield a seriously distorted output waveform for a displacement that exceeds a quarter of a wavelength [11].

Three indices of radar performance are used to measure the percentage detection error, nonlinearity, and speed of the radar. The first index quantifies the percentage detection error, and is defined as the ratio between the root-mean-square (RMS) value of the estimated error and the RMS value of the actual trajectory:

$$\text{Detection error} \stackrel{\text{def}}{=} \frac{\text{RMS of } (x - \hat{x})}{\text{RMS of } x} \times 100\% \tag{22}$$

This index provides convenient yet stringent performance evaluation because any phase mismatch generates a significant error even when the radar produces an output wave-shape that is identical to the actual trajectory. The linearity of the radar is assessed by the total harmonic distortion (THD), defined as the ratio of the RMS value of the sum of all harmonics to the RMS value of the fundamental at the radar output. The THD of the estimated trajectory $\hat{x}$ quantifies the nonlinearity of the radar in sensing a harmonic motion. The radar output in Fig. 6 has a detection error of around 1.4% and a THD of 0.1%.

C. Maximum Detectable Speed

The third performance index is the maximum detectable speed, which quantifies the speed of the radar and is defined as the maximum speed of a moving target that can be detected by the radar with a detection error of less than 5%.

Fig. 7 plots the maximum detectable speed versus the control bandwidth. The solid line shows the maximum allowable speeds predicted by (18), and the circles and asterisks represent the simulated results for sinusoidal and triangular target trajectories, respectively. The sinusoidal trajectory used in the test is $x(t) = X\sin(2\pi \times 10t)$, with a peak instantaneous speed of $2\pi \times 10X$. The test involves gradually increasing the amplitude X until the detection error exceeds 5%. The maximum allowable speed is then recorded as $2\pi \times 10X_{\max}$. For the test of 50Hz triangular trajectories with different amplitudes, the maximum allowable speed corresponds to the largest slope of the triangular trajectory that still yields a detection error of less than 5%.

The simulations yield very interesting results. When the control bandwidth is below 5 kHz, the results of both sinusoidal and triangular tests are as predicted. However, as the control bandwidth increases above 5 kHz, in the sinusoidal test, it still shows a similar upward trend in the maximum allowable speed, but in the triangular test, a saturation occurs as increasing the control bandwidth produces no significant performance improvement. The discrepancy arises from the obvious fact that the triangular trajectory has additional high frequency components that may excite unwanted oscillations in the control system, thereby narrowing its effective operating range and adversely affecting the maximum detectable speed. As the control bandwidth is increased, the effect becomes more pronounced, because the stability of the control system declines and it becomes more oscillatory as a result of a lack of damping. Notice that in Fig. 5, the 5kHz control bandwidth corresponds to a phase margin of 50 degrees and a gain of 1.9. It is consistent with the authors' experience that a feedback system with a phase margin of less than 50 degrees is about to become oscillatory, providing indirect evidence of the accuracy of the model.

The maximum allowable speed may also be called the "amplitude-frequency product" when used as a performance index. From the estimate $v_{\max}$ by (18), we may predict without further simulation that the radar is able to detect simple harmonic motion with amplitude A and a frequency of up to about $v_{\max}/A$ (rad/s). This prediction agrees fairly well with the simulation.

D. Region of Stability

The analysis in Section III suggests that a possible stable operating point for a positive-gain controller is in the range $\theta \in (0.5\pi,\ 1.5\pi)$ in which the plant gain is negative so as to

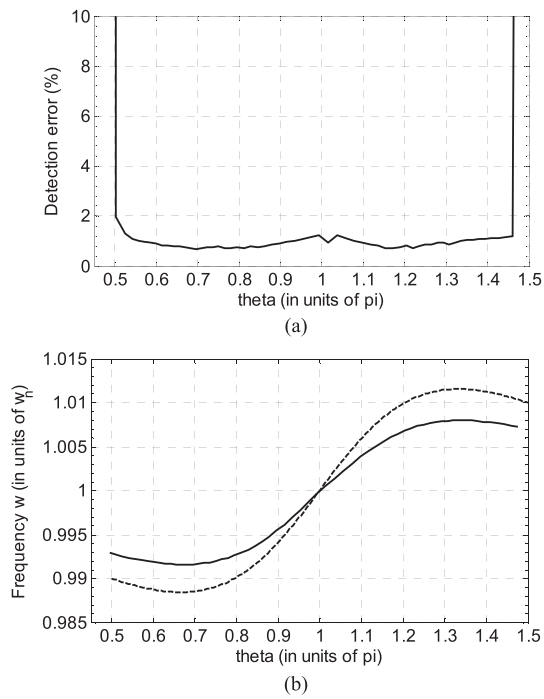

Fig. 8. Simulation results for the SIL radar to sense 10 mm (peak-to-peak), 10 Hz harmonic motion, at different operating points θ: (a) detection error; (b) oscillation frequency ω (dashed: theoretical expectation; solid: simulation).

maintain a negative feedback loop. To verify this assertion and to validate the model, the PI controller given by (20) is used to operate the system at various points, by setting the set-point r to different values. In simulations, the actual ω and θ are recorded by observing the Fourier transforms of u_{out} and u_{inj}, and identifying their fundamental components and the phase difference between them.

Fig. 8 shows the simulated results of the detection of a given trajectory $x = 0.005\sin(2\pi \times 10t)$. The region of stability is $\theta \in [0.5\pi, 1.46\pi]$, in which the detection error is about 1% and beyond which the radar starts to lose control with an abrupt increase in the detection error. The region of stability is close to the prediction; it shrinks a little at the 1.5π end because the phase θ tends to increase as the phase control system becomes closer to unstable, making it easier to get passing of the 1.5π end.

Fig. 8(b) plots the graph of the oscillation frequency ω against the operating point θ. The oscillation frequency, as predicted, equals the free-running frequency ω_n at $\theta = \pi$. The simulated maximum frequency deviation is less than 1%, justifying the assumption of a small frequency deviation that is made to derive the approximate frequency equation (2). (See Appendix A for details.) The frequency shift that is predicted by (2), with the substitution of (A34) and (A35) for amplitudes B and A, is written as

$$\frac{\omega - \omega_n}{\omega_n} = \frac{-A_{inj}\sin(\theta)}{2Q\left[1 + A_{inj}\cos(\theta)\right]}, \quad A_{inj} = 0.5. \tag{23}$$

This equation can be found elsewhere [13]. Fig. 8(b) shows the frequency shift predicted by (23) as a dashed curve, which

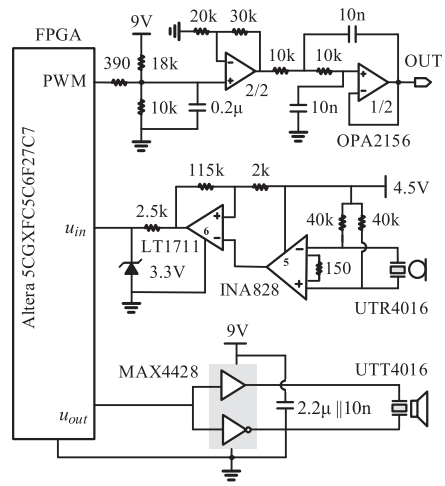

Fig. 9. Analog circuit for the proposed SIL ultrasonic radar. All of the ICs run from a 9 V supply.

does not perfectly match the simulated results, but they exhibit similar trends.

Note that the stable region does not imply that the initial phase $\theta(0)$ of the radar has to be in this region. In fact, the initial position of the target is not important, because if the initial phase is outside the stable region, the phase will quickly grow up and eventually be wrapped back to the stable region. Therefore, after an unnoticed short transient, the regulator is still able to regulate the phase to the desired point $\theta = \pi$.

V. Experimental Result

A. Radar Analog Front-End

The SIL ultrasonic radar, designed in Subsec. IV-A, is constructed in the lab. Fig. 9 presents the analog circuit that interfaces between the FPGA and the ultrasonic transducers. The 40 kHz ultrasonic transducers that are worked with herein are a UTT4016 (transmitter) and a UTR4016 (receiver). The transmitter is driven with a 9 V square wave by an H-bridge class-D amplifier MAX4428, in accordance with the switching command from the FPGA. The reflected ultrasound sensed by the receiver is amplified by an instrumentation amplifier INA828 with a gain of $g = 334$ and is then converted into a square wave by a comparator LT1711, with hysteresis of $h = 0.15$ V. The comparator output is clamped using a 3.3 V Zener diode before it is sent to the SIL oscillator in the FPGA. A third-order lowpass RC op-amp circuit, with a cutoff frequency of 1.5 kHz, demodulates the PWM output signal.

The comparator hysteresis, $h = 0.15$ V, on the one hand avoids erroneous switching caused by noise, but on the other hand sets a minimum operating level, below which there will be no comparator switching and the SIL radar fails to detect the object. So, to maintain the normal function, the radar should at least have the received signal amplitude greater than

$$V_R = 0.5h/g = 0.075/334 = 2.25 \times 10^{-4}\ \text{V}.$$

where g is the amplification gain of the receiver amplifier.

TABLE I
PARAMETERS FOR DETERMINING THE RADAR DETECTION RANGE

Transmitter	Sound pressure level *SPL* (relative to 20 μPa/10 Vrms)	120 dB
	Driving voltage V_T	11.46 V
Receiver	Sensitivity *S* (Vrms/μBar)	-63 dB
	Minimum detectable signal V_R	0.225 mV
Absorption loss	Absorption coefficient α (20°C, RH=50%)	1.256 dB/m
Target	Effective area for reflection A_{obj}	0.06 m^2

The required minimum signal amplitude V_R limits the detectable range of the radar. A new range equation for an ultrasonic radar is presented below (see Appendix D for the derivation):

$$R = \frac{W(0.115\ \alpha R_0)}{0.115\ \alpha}\ \text{m}, \tag{24}$$

where *W*(.) is the Lambert *W* function [33], α is the absorption coefficient of sound propagation in air [29], and R_0 is given by

$$R_0 = \left(2.4 \times 10^{(S+SPL-120)/20}\sqrt{A_{obj}}\frac{V_T}{V_R}\right)^{1/2}. \tag{25}$$

The detection range depends on the transmitter gain *SPL*, the transmitter driving voltage V_T, the receiver sensitivity *S*, the minimum detectable signal amplitude V_R, the absorption coefficient α, and the target's effective area for reflection A_{obj}. The transmitter gain and the receiver sensitivity can be found in the datasheets of the transducers, as listed in Table I. The driving voltage is the fundamental component in the 9 V driving square wave, namely $V_T = 9 \times 4/\pi = 11.46$ V. The absorption coefficient α for the 40 kHz ultrasound in air at 20°C and 50% relative humidity is 1.256 dB/m [29]. Suppose the target to be detected is the human chest and its effective area is about 0.06 m^2. With all these parameters, we can use the lambertw command in MATLAB to find the radar range:

$$\text{R} = \text{lambertw}\,(0.115 * \text{alpha} * \text{R0})\ /\ (0.115 * \text{alpha})$$

The obtained range estimate is 2.9896 m, which is very close to the measured radar range 2.97 m, as will be shown later. This simple radar range equation offers a surprisingly accurate prediction.

B. FPGA Implementation

The core circuit of the SIL radar is implemented on an Altera FPGA 5CGXFC5C6F27C7. All of the transfer functions that were designed in Subsection IV-A are converted from continuous time to discrete time. Fig. 10 displays the schematic diagram of the SIL oscillator operated at 10 MHz. The 40 kHz resonator, with $Q = 25$, is realized by the feedback connection of a first-order lowpass filter G_1 and an integrator G_2. G_1 and G_2 are triggered at the different edges of the clock signal to create a delay for the causality of the feedback loop. All the gains and filter coefficients in Fig. 10 are implemented by shifts and adds [30]. The demodulating filter *F* in (19) is decomposed into

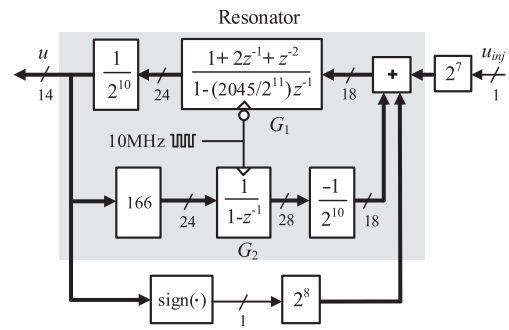

Fig. 10. FPGA implementation of the SIL oscillator.

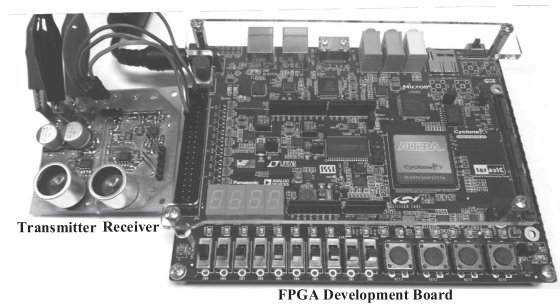

Fig. 11. Radar transceiver circuit board and FPGA board.

two second-order filters, one with a higher cutoff frequency of 19 kHz is sampled at 1 MHz, and the other with a lower cutoff frequency 13 kHz is sampled at 250 kHz. They perform the down-sampling and lowpass filtering of $u(t)u(t\text{-}T/4)$, to extract the frequency shift from the oscillator output *u*. The PI controller of the gains in (20) is sampled at 50 kHz, and has the same clock frequency as the PWM. A 40000-bit shift register, clocked at 50 MHz, is used to implement the tunable delay circuit. Each clock pulse shifts the data in the shift register by one bit. The data in the shift register is then addressed by the quantized output of the PI controller. The resolution of the delay times is set by the clock period, $d_{\min} = 20$ ns, and the maximum delay that may be provided depends on the number of bits, $d_{\max} = 40000 \times 20$ ns $= 0.8$ ms; together, they determine the resolution and range of detectable target motions. According to (5), we have

$$\text{Resolution } = 0.5c \times d_{\min} = 3.4\ \mu\text{m};$$

$$\text{Range of motion} = 0.5c \times d_{\max} = 136\ \text{mm}.$$

C. Linearity Test

Fig. 11 shows the circuit boards of the ultrasonic radar. To test the radar, linear actuators X-LSQ150D (with higher speed) and A-LSQ150A (with higher resolution) are used to create different motions for a 0.2 m × 0.3 m reflection board, and a data acquisition module, cDAQ-9171, is used to record the radar output signals. First, the basic function of the radar is tested. Fig. 12 shows the signals of the radar in detecting an

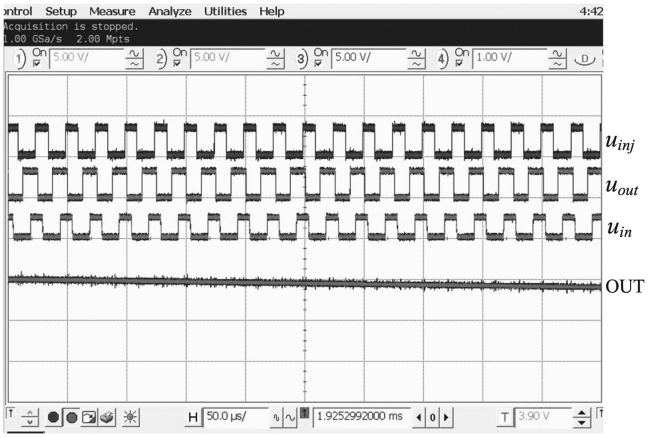

Fig. 12. Oscilloscope graph of the signals of the radar in sensing a quickly approaching hand.

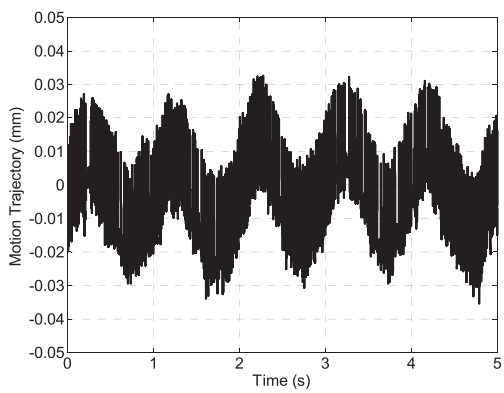

Fig. 13. Motion trajectory determined by the ultrasonic radar in detecting a 1 Hz harmonic motion of amplitude 0.01 mm.

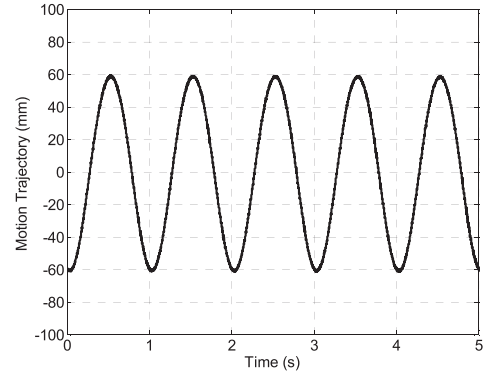

Fig. 14. Motion trajectory determined by the ultrasonic radar in detecting a 1 Hz harmonic motion of amplitude 60 mm.

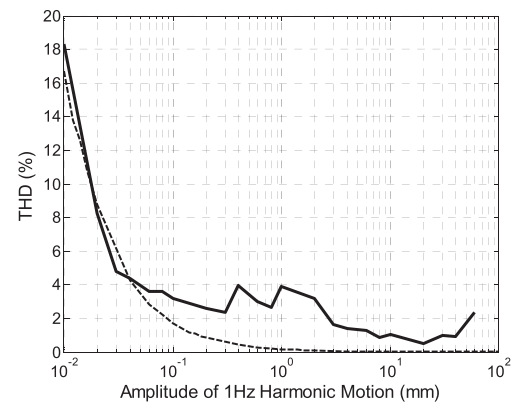

Fig. 15. THD of the output of radar used to sense 1 Hz harmonic motions of various amplitudes (solid: measurement; dashed: simulation).

approaching hand. As expected, the phase between the received signal u_{in} and the transmitted u_{out} varies accordingly with the hand motion, and so does the radar output signal OUT. Due to the phase regulation, the phase between u_{inj} and u_{out} keeps a constant value around 180 degrees, unaffected by the phase change of the received echo u_{in}. One can also notice that the duty cycle of the u_{in} is slightly deviated from 50%, due to the dc offset of the receiver amplifier. However, it does not affect the detection accuracy, because the resonator in the SIL oscillator will filter out the dc offset or other out-of-band noise. This demonstrates the high tolerance of the SIL radar to circuit non-idealities.

The second experiment is to measure the maximum detection range of the radar. The radar is placed 3.5 meters away from the reflection board that performs 1 Hz, 10 mm harmonic motion. As expected, the radar output does not have any response. Slowly move the radar closer to the target until it begins to respond, and then record the distance. After repeating the measurements five times, we get the average range 2.97 m, which is very close to the value 2.9896 m predicted by the radar range equation (24).

The third experiment is to find the smallest movement that can be detected from the noise. Fig. 13 shows the result of the detection of a 1 Hz harmonic motion of amplitude 10 μm, 30 cm away from the radar. The radar output has a THD of up to 18.3%. Although the detected motion includes about 26 μm peak-to-peak noise (majorly due to the finite resolution of the variable delay as will be shown later), we have no difficulty in differentiating between the expected 1 Hz sine wave and the noise. The next test is performed to find the largest displacement that can be detected without obvious distortion. Fig. 14 displays the radar output waveform in the detection of a 1 Hz harmonic motion with an amplitude of 60 mm. Even with a peak-to-peak motion of 120 mm (a distance of about 14 wavelengths of the 40 kHz ultrasound), the radar output has a THD of only 2.3%. The achievable resolution and range for motion detection are pretty close to theoretical predictions.

Next, the linearity of the radar in sensing different harmonic motions is evaluated. The first test is a constant frequency test. Fig. 15 plots the total harmonic distortion of the radar output in the detection of 1 Hz motions of various amplitudes. The measured results are highly consistent with the simulation results when the motion amplitudes are less than 0.05 mm. This agreement suggests that the increase in distortion is mostly caused by the limited resolution of the radar (set by the clock period of the shift register), and not by imperfections of the circuit and the noise. In detecting larger movements, the radar

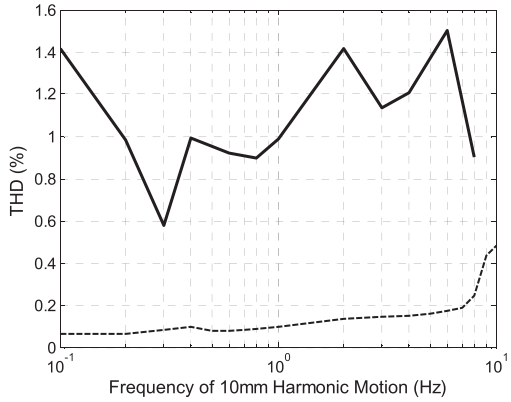

Fig. 16. THD of the output of radar used to sense 10 mm harmonic motions of various frequencies (solid: measurement; dashed: simulation).

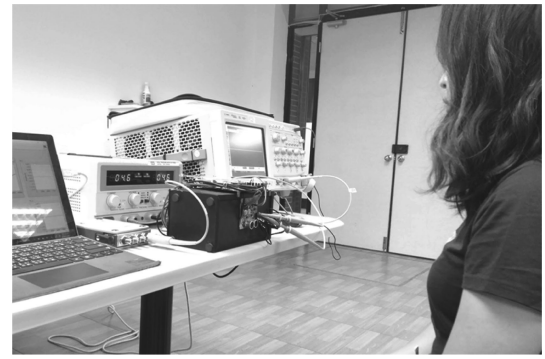

Fig. 17. Experimental setup.

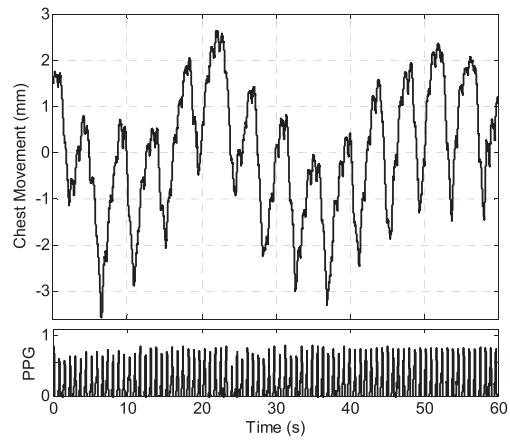

Fig. 18. Detected chest movement and PPG signal.

exhibits better linearity, but the measured THDs are still higher than predicted by simulation; according to observations, the extra distortion arises largely from the actuator nonlinearity and in part from the circuit and ambient noise. The measured THD values are less than 4% for amplitudes from 0.05 mm to 60 mm. The test is performed only to 60 mm because this is the maximum amplitude that can be generated for 1 Hz harmonic motion without losing motor steps on our linear stage. The second test is the constant amplitude test, involving harmonic motions with a fixed amplitude of 1 cm but different frequencies. Fig. 16 plots THD against motion frequency. The simulation reveals that the harmonic distortion increases with the frequency, because the controller gains are lower at higher frequencies. However, the measurements reveal no such relationship because non-idealities of the circuit and the actuator dominate the small control error. Our intent was to test the radar bandwidth by increasing the frequency of motion until the radar failed to detect it. However, the test could be performed only up to a frequency of 8 Hz, which is the maximum frequency that the actuator could reach for a harmonic motion with an amplitude of 1 cm. Nevertheless, we can still infer from the experiments that the SIL radar with proposed feedback demodulation exhibits high linearity over a wide sensing range. By contrast, the same 40 kHz ultrasonic radar with direct demodulation will become seriously distorted in detecting a motion with an amplitude of greater than 1.1 mm (with a total displacement of more than $\lambda/4 = 2.125$ mm).

D. Non-Contact Monitoring of Respiration and Heartbeat

The ultrasonic radar is used to detect the chest movement of a 50 year-old male adult at a distance of 30 cm, to monitor both respiration and heartbeat. The experimental setup is like Fig. 17. Fig. 18 plots the result of detection by the radar. The chest movement consists of small involuntary body movements and two almost periodic patterns—breathing (at lower frequency and with the larger amplitude) and heartbeat (at higher frequency and with the smaller amplitude). The displacement associated with breathing is roughly 2.5 mm, and that associated with the heartbeat is about 0.2 mm. The maximum instantaneous speed of the chest motion is about 0.04 m/s, far below the theoretically maximum detectable speed 20.4 m/s of the designed radar. With the help of the proposed feedback demodulation scheme, the SIL ultrasonic radar faithfully detects the chest movement, whose associated signal would otherwise be seriously distorted as a result of unavoidable null points in the detection of movement of more than a quarter of a wavelength. It is more difficult to recognize the heartbeat pattern than the obvious respiratory rhythm. The estimation of heart rate is more prone to error, so a photoplethysmographic (PPG) sensor is placed on the forefinger of the examinee to measure the arterial pulses, as a reference to verify the heat rate that is measured by the radar. Fig. 19 displays the power spectrum from one minute of chest movement data, shown in Fig. 18. The lack of intermodulation distortion enables the respiratory rate of 14 breaths per minute and the heart rate of 83 beats per minute (BPM) to be easily determined from the fundamental frequencies of the breathing and heartbeat rhythms. The estimated heart rate is very close to the heart rate of 82.4 BPM that is determined from the PPG measurement. Table II shows the heart rate measurements for four examinees. Each examinee is tested ten times, and the average heartrate error and the standard deviation are recorded. The brassiere on the woman examinee does not seem to affect the radar detection. The

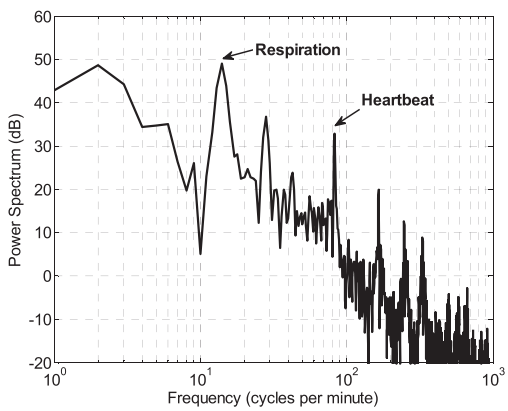

Fig. 19. Power spectrum of the detected chest movement.

TABLE II
HEART RATE ERROR AND STANDARD DEVIATION (IN BPM)

Examinee	Male 50 y/o	Female 41 y/o	Male 24 y/o	Male 25 y/o
Absolute average error	0.33	0.52	0.23	0.38
Standard deviation	0.78	1.17	0.81	0.92.

results show consistent small heart rate errors for all examinees, confirming the accuracy of the radar's heart rate detections.

More experiments are carried out to examine the interference effects of other objects near the radar on its sensing accuracy. First, due to the directional property of the transducers (with the beam angle of about 55°), people walking or hand waving on the two sides of the examinee does not affect much, only creating about 0.1 mm of perturbation on the radar output trajectory. People walking behind the examinee will affect the sensing accuracy more; it may create a trajectory perturbation as large as 0.5 mm, larger than the rhythm created by heartbeat. Third, the stationary object that partially blocks the chest will weaken the sensed motion signal, as a result of the combination of the two echoes that reduces the Doppler phase shift induced by the chest motion. The more blocking will lead to more shrinkage in the displacement measured by the radar.

VI. CONCLUDING REMARKS

This is the first paper to report an SIL ultrasonic radar for non-contact monitoring of respiration and heartbeat. All of the previously reported SIL radars are on microwave because the 1/4-wavelength limitation on the motion sensing makes it harder to find a practical use on ultrasound with a comparatively shorter wavelength. The proposed phase-canceling feedback demodulation scheme for extracting the target motion greatly enhances the linearity of an SIL radar and makes it possible to detect large chest movements without significant distortion, thus allowing accurate measurements of the respiration rate and heart rate. The radar has a very wide linear sensing range, up to 14 wavelengths. But this is not a physical limitation. An even wider sensing range and higher resolution can be achieved using an FPGA with more gate elements and a higher clock rate.

Table III reveals that for vital sign detection applications the developed SIL ultrasonic radar outperforms the other ultrasonic or microwave Doppler radars in terms of the detected maximum peak-to-peak displacement. For fair comparisons, all the distances and displacements shown in Table III are normalized by the wavelengths. The attractive features of the proposed phase-canceling SIL radar are emphasized here. First, as a result of injection locking to enhance the phase SNR [9], the proposed radar has better immunity to phase noise than the Doppler radars. Second, the proposed phase-canceling radar has a much wider sensing range than the phase-tracking radar, which, when used for the same 40 kHz ultrasonic application, can detect a maximum displacement of about two wavelengths, since commercial 40 kHz ultrasonic transducers commonly have a bandwidth of only 2 kHz, which sets the maximum tunable range for the phase-tracking radar. Third, among the three radars, the arctangent-demodulation Doppler radar is the most sensitive to circuit imperfections (such as dc offset and quadrature channel imbalance [18], [20]). Our phase-canceling SIL radar and the phase-tracking radar need only a single channel for demodulation and so do not have the problem of channel imbalance, and the dc offset affects only the operating point of the radar but not its sensing accuracy if the feedback loop is stable. In summary, high noise immunity, a wide linear sensing range, and good tolerance of circuit imperfections are nice properties of the proposed SIL radar. Despite all of the promising results in this investigation, the following points merit further discussions.

1) *(Validity of the model):* Some may argue that since Adler's phase equation is derived based on the assumption that the injection level is small and barely influences the oscillation amplitude [12], [14], the model of the SIL radar derived from it will inherit that restriction, and so may not apply to a large injection as suggested in our design. To dispel this doubt, Appendix A derives the equations for oscillation frequency and amplitude by only assuming at the outset that the phase varies much more slowly than the oscillation frequency, $|\theta'| \ll \omega$. The obtained frequency equation is exactly the same as that derived from Adler's equation. The frequency and amplitude equations (A14) and (A19) are not limited to a small injection. The validity and adequacy of the plant model are also confirmed by the well-designed tests.
2) *(Instability of the anti-phase mode):* Another concern may arise from the fact that the anti-phase injection mode of operation ($\theta = \pi$) of the SIL oscillator that is used here is unstable [15], so it is impossible to operate the radar in its anti-phase mode by carefully setting a "fixed" delay or phase lag in the signal return path. Yes, indeed. The instability of this mode of operation can also be inferred as follows: by (A14), at $\theta = \pi$, a slight increase in θ results in an increase in ω, which in turn causes another increase in θ, as suggested by (A23). This positive feedback results in the instability of the anti-phase injection mode. However, the proposed feedback tuning of the delay alters the

TABLE III
PERFORMANCE COMPARISON

Reference	Proposed phase-cancelling SIL radar	Phase tracking Doppler radar [2-4], [7]		Arctangent-demodulation Doppler radar [18,19, 21, 22]
Wave characteristics	Ultrasound, longitudinal wave	Ultrasound, longitudinal wave	Microwave, transverse wave	Microwave, transverse wave
Frequency/ wavelength (λ)	40 kHz/8.6 mm	[2] 900 kHz/0.38 mm [3] 40 kHz/8.6 mm [4] 40 kHz/8.6 mm	[7] 5.8 GHz/51.7 mm	[18], [22] 2.4 GHz/125 mm [19] 5.8 GHz/51.7 mm [21] 20 GHz/15 mm
Detectable vital signs	RR/HR	[2] PR [3] RR*/HR* [4] RR	[7] RR/HR	RR/HR
Target's distance from radar	300 mm/34.9 λ	[2] 15 mm/39.5 λ [3] N.A. [4] N.A.	[7] 2000 mm/38.7 λ	[18] 1000 mm/8 λ [19] 2000 mm/38.7 λ [21] 1000 mm/66.7 λ [22] 250 mm/2 λ
Detected maximum peak-to-peak displacement	120 mm/14 λ	[2] 1 mm/2.56 λ [3] N.A. [4] N.A.	[7] 2.1 mm/0.04 λ	[18] N.A. [19] 20 mm/0.39 λ [21] 12 mm/0.8 λ [22] 450 mm/3.6 λ

Notes: RR, HR and PR denote respiration rate, heart rate and pulse rate, respectively. * No experimental results

positive feedback nature and makes possible this mode of operation.

3) *(Correction for demodulation error):* In some cases, due to the limited memory and precision, the delay time of the digitally implemented *T*/4 delay block in the demodulator may have a small error. This time delay error generates a dc offset at the FM demodulator output and unintentionally causes a change in the operating point. As noted in Appendix C, the time delay error in the *T*/4 delay block results in an approximately equal percentage frequency shift. Consider our design as an example: the maximum frequency deviation is less than 1% as shown in Fig. 8(b). Therefore, a 1% error in the delay time of the *T*/4 delay block is enough to steer the operating point out of the region of stability and cause failure of the phase control. Fortunately, the problem can be easily remedied by setting the set-point *r* as in (A39). This nonzero set-point value corrects the dc error at the demodulator output and keeps the SIL radar working properly at the desired operating point.

4) *(Feedback of amplitude):* Since both the oscillation frequency and amplitude change with the phase θ, phase control can also be performed by demodulating the amplitude from the oscillation signal and then using it as a feedback signal. Then, with the proper setting of *r*, the phase θ can be regulated to the desired point. The amplitude demodulation is easy, and can be done by passing u^2 through a lowpass filter (by simply replacing the *T*/4 delay block by a unity gain in Fig. 2). However, amplitude feedback, as revealed by the amplitude equation (A19), has a troublesome implication, especially for those seeking very high-bandwidth sensing of motion: the amplitude feedback adds an additional first-order lowpass dynamics (with a cutoff frequency of about $f_n/(2Q) = 800$ Hz in our example) to the plant model, which seriously limits the control bandwidth and thus render the performance less satisfactory than that achieved by feeding back the frequency shift as in the proposed design.

APPENDIX

A. Equations of Slowly Varying Frequency and Amplitude

The frequency and amplitude of the SIL oscillator are affected by the phase difference θ between the oscillator output signal and the injected signal. With reference to Fig. 1, the resonator output *u* and its instantaneous frequency ω are expressed as

$$u(t) = A(t)\cos[\omega_n t + \phi(t)], \tag{A1}$$

$$\omega(t) = \omega_n + d\phi(t)/dt. \tag{A2}$$

Assume that the resonator has a high-Q second-order bandpass response and a unity peak gain, and satisfies the following differential equation:

$$u''(t) + \tfrac{\omega_n}{Q}u'(t) + \omega_n^2 u(t) = \tfrac{\omega_n}{Q}u_1'(t). \tag{A3}$$

The resonator input u_1 is a combination of two signals–a square wave u_{out} with a normalized amplitude of 1 and an injected sine wave u_{inj} with an amplitude of *B*. Due to its narrow bandwidth, the resonator rejects most high-frequency switching harmonics, and only the fundamental component of the square wave has to be considered. That is,

$$u_1(t) = \tfrac{4}{\pi}\cos[\omega_n t + \phi(t)] + B\cos[\omega_n t + \phi(t) - \theta(t)]. \tag{A4}$$

The equality in (A4) is sloppy but should not cause any confusion, on the understanding that only approximate equations are derived. Substituting (A1), (A2), and (A4) into (A3) yields

$$f(t) = g(t)\cos(\omega_n t + \phi) - h(t)\sin(\omega_n t + \phi) = 0, \tag{A5}$$

where

$$g(t) = A'' + \tfrac{\omega_n}{Q}A' + (\omega_n^2 - \omega^2)A + \tfrac{\omega_n B}{Q}\sin(\theta)(\theta' - \omega) \tag{A6}$$

$$h(t) = 2\omega\left[A' + \left(\tfrac{\omega'}{2\omega} + \tfrac{\omega_n}{2Q}\right)A + \tfrac{\omega_n B}{2Q}\cos(\theta)\left(\tfrac{\theta'}{\omega} - 1\right) - \tfrac{2\omega_n}{\pi Q}\right] \tag{A7}$$

The target is assumed to move so slowly relative to the carrier frequency ω that the resulting rate of change of the phase satisfies

the condition:

$$|\theta'|/\omega \ll 1. \tag{A8}$$

As the phase θ varies slowly, so do the oscillation frequency ω and amplitude A. Therefore, it is reasonable to assume $g(t)$ and $h(t)$ in (A5) being almost constant in a period T of oscillation. With this assumption, we can get the low-frequency dynamic equations of ω and A by taking the following averages of (A5) over a period T of oscillation.

$$0 = \frac{2}{T}\int_{t-T/2}^{t+T/2} f(\tau)\cos[\omega_n\tau + \phi(\tau)]d\tau \approx g(t); \tag{A9}$$

$$0 = \frac{2}{T}\int_{t-T/2}^{t+T/2} f(\tau)\sin[\omega_n\tau + \phi(\tau)]d\tau \approx h(t); \tag{A10}$$

which give two nonlinear differential equations:

$$A'' + \tfrac{\omega_n}{Q}A' + (\omega_n^2 - \omega^2)A + \tfrac{\omega_n B}{Q}\sin(\theta)(\theta' - \omega) = 0; \tag{A11}$$

$$A' + \left(\tfrac{\omega'}{2\omega} + \tfrac{\omega_n}{2Q}\right)A + \tfrac{\omega_n B}{2Q}\cos(\theta)\left(\tfrac{\theta'}{\omega} - 1\right) - \tfrac{2\omega_n}{\pi Q} = 0. \tag{A12}$$

The original almost equal signs have been replaced by equality signs. Once again, this slight abuse of equality is convenient, on the understanding the equations are only approximate.

The static solution for ω is obtained by substituting $A'' = A' = \theta' = 0$ into (A11).

$$(\omega - \omega_n)\left(1 - \tfrac{\omega - \omega_n}{2\omega}\right) = -\tfrac{\omega_n B}{2QA}\sin(\theta). \tag{A13}$$

Since the bandwidth of the resonator is narrow, the percentage change in the oscillation frequency is very small (less than 1% in our design example), so (A13) can be well approximated by

$$\textbf{frequency equation}: \omega - \omega_n = -\tfrac{\omega_n B}{2QA}\sin(\theta). \tag{A14}$$

The static solution for ω is exactly the same as that derived from Adler's equation [9]. Similarly, the static solution for θ can be obtained from (A12) by setting $A' = \omega' = \theta' = 0$:

$$A = B\cos(\theta) + \tfrac{4}{\pi}. \tag{A15}$$

An important question immediately arises: are there any essential dynamics missing from this static model due to the oversimplification of Adler's equation? Can we obtain more accurate linear dynamic equations for ω and A from the nonlinear differential equations (A11) and (A12)?

We attempt to simplify (A11) and (A12) by removing insignificant terms, based on the previously made assumption in (A8). Assume that no resonance peaks of the responses of ω and A are present in the low-frequency band where the target motion is to be detected, so the magnitudes of ω' and A' can be roughly estimated from their static expressions in (A14) and (A15) without creating huge errors. Since the injection amplitude B is constant in the design, the following estimate is obtained from (A15).

$$A' \approx -B\sin(\theta)\theta'. \tag{A16}$$

Similarly, differentiating (A14) with respect to time and substituting (A16) into it yields the following rough estimate

$$|\omega'| \approx \tfrac{\omega_n}{2Q}\tfrac{B}{A}\left|\cos(\theta) + \tfrac{B}{A}\sin^2(\theta)\right||\theta'|. \tag{A17}$$

From (A8) and (A17), we can infer that the following term in (A12) is insignificant.

$$\tfrac{|\omega'|}{2\omega} \approx \tfrac{\omega_n}{2Q}\tfrac{B}{A}\left|\cos(\theta) + \tfrac{B}{A}\sin^2(\theta)\right|\tfrac{|\theta'|}{2\omega} \ll \tfrac{\omega_n}{2Q}. \tag{A18}$$

With the insignificant terms removed, (A12) can be approximated by a first-order differential equation

$$\textbf{amplitude equation}: A' + \tfrac{\omega_n}{2Q}A = \tfrac{\omega_n B}{2Q}\cos(\theta) + \tfrac{2\omega_n}{\pi Q}. \tag{A19}$$

The amplitude exhibits lowpass behavior with a cutoff frequency of $\omega_n/(2Q)$ rad/s.

In an analogous manner, a simplified equation for ω can be obtained. First, taking the time derivative of (A19) yields

$$A'' + \tfrac{\omega_n}{2Q}A' = -\tfrac{\omega_n B}{2Q}\sin(\theta)\theta'. \tag{A20}$$

Then, subtracting (A20) from (A11) gives

$$\omega - \omega_n \approx \tfrac{\omega^2 - \omega_n^2}{2\omega} = \tfrac{\omega_n}{2Q}\left[\tfrac{B\sin(\theta)}{A}\left(\tfrac{\theta'}{2\omega} - 1\right) + \tfrac{A'}{2\omega A}\right]. \tag{A21}$$

Also according to (A8) and (A16), following small terms in square brackets in (A21) can be neglected.

$$\tfrac{|A'|}{2\omega A} \approx \tfrac{B|\sin(\theta)|}{A}\tfrac{|\theta'|}{2\omega} \ll \tfrac{B|\sin(\theta)|}{A}. \tag{A22}$$

Removing the insignificant terms from (A21) yields the same equation (A14) as that derived from Adler's equation. So indeed the frequency and amplitude equations (A14) and (A19) adequately describe ω in the low-frequency band of interest.

B. Derivation of Plant Model

A small-signal plant model for the SIL radar is derived here. The plant input is the tunable delay d and the plant output is the demodulator output w.

With reference to Fig. 2, the phase θ between the oscillator square-wave output u_{out} and the injected square wave u_{inj} is determined by the round-trip delay D and the tunable delay d. Since the oscillator output u_{out} is in phase with u in (A1), the phase θ is the difference between the angle in the cosine function in (A1) and that in its (D+d)-delayed version, as below.

$$\begin{aligned}\theta(t) &= [\omega_n t + \phi(t)] - [\omega_n(t - D - d) + \phi(t - D - d)]\\ &= \omega_n(D + d) + [\phi(t) - \phi(t - D - d)]\\ &\approx [\omega_n + \phi'(t)](D + d)\\ &= \omega(t)(D + d)\end{aligned} \tag{A23}$$

Since ω deviates from ω_n only very slightly, the variation of the phase θ is approximately related to the variation of the tunable delay d by

$$\delta\theta/\delta d \approx \omega_n, \tag{A24}$$

where δ denotes a small change in a quantity.

Equation (2) describes the relationship between the injection phase lag θ and the frequency shift $\Delta\omega = \omega - \omega_n$. A small

perturbation on θ results in a variation of $\Delta\omega$ in (2).

$$\Delta\omega + \delta\Delta\omega = -\frac{\omega_n B}{2QA}\sin(\theta + \delta\theta), \tag{A25}$$

where $\delta\Delta\omega$ means a small variation in the frequency shift. Expanding (A25) and making some approximations yields

$$\Delta\omega + \delta\Delta\omega \approx -\frac{\omega_n B}{2QA}\sin(\theta) - \frac{\omega_n B}{2QA}\cos(\theta)\delta\theta. \tag{A26}$$

Subtracting (2) from (A26) gives

$$\frac{\delta\Delta\omega}{\delta\theta} \approx -\frac{\omega_n B}{2QA}\cos(\theta). \tag{A27}$$

We now need to derive the relationship between the oscillation frequency ω and the FM demodulator output w. The demodulator extracts the frequency shift, $\Delta\omega = \omega - \omega_n$, from the resonator output signal u in (A1). With $T = 2\pi/\omega_n$, the $T/4$ delay block in Fig. 2 converts signal u from a cosine function into a sine function. The multiplier performs the computation:

$$\begin{aligned} u(t)u\left(t - \tfrac{T}{4}\right) &= A^2\cos[\omega_n t + \phi(t)]\sin\left[\omega_n t + \phi\left(t - \tfrac{T}{4}\right)\right] \\ &= \tfrac{A^2}{2}\left\{\sin\left[2\omega_n t + \phi(t) + \phi\left(t - \tfrac{T}{4}\right)\right] - \sin\left[\phi(t) - \phi\left(t - \tfrac{T}{4}\right)\right]\right\}, \end{aligned} \tag{A28}$$

which, if followed by an ideal lowpass filter, gives

$$w(t) = \mathrm{LP}\left\{u(t)u\left(t - \tfrac{T}{4}\right)\right\} = \tfrac{-A^2}{2}\sin[\phi(t) - \phi(t - \tfrac{T}{4})], \tag{A29}$$

where, according to (A2), the argument of the above sine function is related to the frequency shift by

$$\phi(t) - \phi\left(t - \frac{T}{4}\right) \approx \frac{T}{4}\frac{d\phi(t - T/8)}{dt} = \frac{\pi}{2}\frac{\omega(t - T/8) - \omega_n}{\omega_n}. \tag{A30}$$

As before, since the frequency deviation is very small, the angle in the sine function in (A29) is very small, and so the demodulator output w can be further approximated by

$$w(t) \approx -\tfrac{\pi A^2 \Delta\omega(t - T/8)}{4\omega_n}. \tag{A31}$$

Taking into account the dynamics of a non-ideal demodulating lowpass filter $F(s)$, the approximate transfer function from $\Delta\omega$ to w is obtained:

$$\frac{\mathcal{L}\{\delta w(t)\}}{\mathcal{L}\{\delta\Delta\omega(t)\}} = \frac{\mathcal{L}\{w(t)\}}{\mathcal{L}\{\Delta\omega(t)\}} \approx \frac{-\pi A^2}{4\omega_n}e^{-s\frac{T}{8}}F(s), \tag{A32}$$

where $\mathcal{L}\{\cdot\}$ is the Laplace transform.

Combining (A24), (A27), and (A32), yields a small-signal model as follows.

$$P(s) = \frac{\mathcal{L}\{\delta w(t)\}}{\mathcal{L}\{\delta d(t)\}} \approx \frac{\pi AB}{8Q}\omega_n\cos(\theta)e^{-s\frac{T}{8}}F(s) \tag{A33}$$

Our design uses a square wave u_{inj} as the injected signal and the amplitude of the injected square wave is A_{inj}. Amplitude B in (A33) is the effective amplitude of the injected square-wave signal u_{inj} that is seen by the resonator, and approximately equals the amplitude of the fundamental component in u_{inj}. Namely,

$$B = \frac{4}{\pi}A_{inj} \tag{A34}$$

Also the oscillation amplitude A can be approximated by (A15) with the substitution of (A34) into it.

$$A = \tfrac{4}{\pi}\left[A_{inj}\cos(\theta) + 1\right]. \tag{A35}$$

Finally, the substitution of (A34) and (A35) into (A33) gives the plant model

$$P(s) = \frac{2A_{inj}\cos(\theta)[1 + A_{inj}\cos(\theta)]\omega_n}{\pi Q}e^{-s\frac{T}{8}}F(s). \tag{A36}$$

C. Error Analysis for the T/4 Delay Block

Suppose there is a time delay error $\Delta\tau = \tau - T/4$ in the $T/4$ delay block of the FM demodulator in Fig. 2. This time delay error will produce an additional dc offset at the demodulator output and unintentionally change the operating point, resulting in performance degradation or even instability. The demodulator output w can be derived, as in (A29), by (A1) and (A2).

$$\begin{aligned} w(t) &= \mathrm{LP}\left\{u(t)u(t - \tau)\right\} \\ &= \tfrac{-A^2}{2}\sin[\phi(t) - \phi(t - \tau) + \Delta\tau\omega_n] \\ &\approx -\tfrac{A^2}{2}\sin\left\{\frac{\pi}{2}\left[\frac{\omega(t) - \omega_n}{\omega_n} + \frac{\Delta\tau}{T/4}\right]\right\}. \end{aligned} \tag{A37}$$

With set-point $r = 0$, the controller regulates the demodulator output w to zero, resulting in

$$\frac{\Delta\tau}{T/4} \approx -\frac{\omega(t) - \omega_n}{\omega_n}. \tag{A38}$$

The time delay error $\Delta\tau$ will result in approximately the same percentage of the frequency shift $\Delta\omega$, which can be translated to a shift in the operating point θ by (A14)

A simple remedy to this problem is to set a nonzero set-point that cancels the dc offset at the demodulator output and corrects the operating point back to the desired $\theta = \pi$, steering the oscillation frequency ω back to ω_n. The required set-point value can be estimated by equating the regulation error to zero, i.e., $w + r = 0$, and making use of (A37) with $\omega = \omega_n$.

$$r = -w \approx \pi A^2\frac{\Delta\tau}{T}. \tag{A39}$$

D. Ultrasonic Radar Equation

As the sound travels, the sound pressure is gradually reduced due to the sound spreading and the absorption loss [29], [31]. We first estimate the received signal level of an ultrasonic radar by an idealized sound propagation model, which assumes that the sound waves produced by the transmitter are spreading out uniformly and losslessly in the cone of a sphere, as illustrated in Fig. 20. Later, we modify the radar signal estimation by taking the absorption loss into consideration.

Ultrasonic transducers are commonly characterized by their transmitting sound pressure p_T at a distance $d = 0.3$ m. The total radiated sound power can be estimated by the transmitting sound pressure and the beam angle θ by the following formula [31], [32],

$$P_{\text{source}} = \frac{A_T p_T^2}{Z} = \frac{2\pi d^2[1 - \cos(0.5\theta)]p_T^2}{Z}\ (\mathrm{W}). \tag{A40}$$

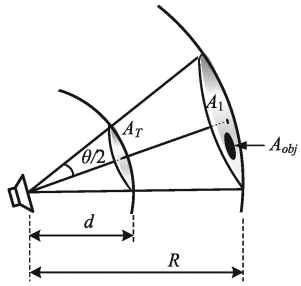

Fig. 20. Idealized sound propagation model: The sound power is radiated in a beam with an angle θ, and spreading out uniformly and losslessly in the cone of a spherical towards an object of an effective area A_{obj}.

where $A_T = 2\pi d^2[1-\cos(0.5\theta)]$ is the area of the spherical cap of the sound beam over which the energy is distributed at the distance *d* from the transmitter, as illustrated in Fig. 20, and *Z* is the acoustic impedance for air. Assume there is an object at the distance *R*. Then, under the assumption of the uniform spherical spreading of the sound without the absorption loss, the acoustic power reaching the object depends on a ratio of the object's effective area A_{obj} and the dome area A_1 of the sound beam in Fig. 20

$$P_{obj} = \frac{A_{obj}}{A_1} P_{\text{source}} = A_{obj} \frac{d^2 p_T^2}{R^2 Z} \ (\text{W}). \tag{A41}$$

Due to more than thousandfold mismatch of the acoustic impedances of air and the object like the human chest [34], it is rational to assume that the acoustic power seen by the object is completely reflected and scattered, spreading uniformly in one direction up to a half-space towards the radar. Hence, the portion of sound power received by the ultrasonic receiver depends on the ratio between the receiver area A_R and the half sphere area $A_2 = 2\pi R^2$.

$$P_{\text{receiver}} = \frac{A_R}{A_2} P_{obj} = A_R A_{obj} \frac{d^2 p_T^2}{2\pi R^4 Z} \ (\text{W}). \tag{A42}$$

Once again, the sound power is related to the sound pressure by the formula, $P = (A\,p^2)/Z$. So, the sound pressure p_R seen by the receiver is

$$p_R = \sqrt{\frac{Z}{A_R} P_{\text{receiver}}} = \frac{d}{R^2}\sqrt{\frac{A_{obj}}{2\pi}} p_T \ (\text{Pa}). \tag{A43}$$

Given the transmitting sound pressure level *SPL* in dB, relative to 20 μPa per 10 V_{rms}, we have the sound pressure p_T produced by the driving voltage V_T, given by

$$\begin{aligned} p_T &= \frac{V_T}{10} \times 10^{SPL/20} \times 20 \times 10^{-6} \\ &= 2 \times 10^{(SPL-120)/20} V_T \ (\text{Pa}). \end{aligned} \tag{A44}$$

Suppose that the sensitivity of the receiver is *S*, volt per microbar, meaning that it produces an output signal of *S* volts for 1 microbar (0.1 Pa) of sound pressure. So the output voltage of the receiver can be predicted by the sound pressure impinging upon it.

$$V_R = 10 \times 10^{S/20} p_R \ (\text{V}). \tag{A45}$$

Substitution of (A43) and (A44) into the above equation yields an estimate for the received signal under no absorption loss:

$$V_R = 8 \times 10^{(S+SPL-120)/20} \frac{d\sqrt{A_{obj}}}{R^2} V_T \ (\text{V}). \tag{A46}$$

Extensive measurements of absorption losses have been made, and the loss is given as an absorption coefficient α [29], defined as the amount of attenuation in sound pressure per meter, in dB/m. Including the absorption coefficient in the signal calculation, we have the *radar signal equation*

$$V_R = 8 \times 10^{(S+SPL-120-2R\alpha)/20} \frac{d\sqrt{A_{obj}}}{R^2} V_T \ (\text{V}). \tag{A47}$$

On the other way around, we may estimate the detection range *R*, given the minimum detectable signal V_R. Plugging the value $d = 0.3$ into the above radar signal equation and rearranging it yields the equation

$$R = R_0 10^{-0.05\alpha R}, \tag{A48}$$

where R_0 is the range estimation from (A46) with zero absorption loss, given by

$$R_0 = \left(2.4 \times 10^{(S+SPL-120)/20} \sqrt{A_{obj}} \frac{V_T}{V_R}\right)^{1/2}. \tag{A49}$$

The nonlinear equation (A48) looks very similar to the famous equation introduced by J. H. Lambert [33]:

$$W(t) = te^{-W(t)}, \tag{A50}$$

where the solution *W*(*t*) is known as the Lambert *W* function. Our equation (A48) can be rewritten in the same form as (A50):

$$0.05\ln(10)\alpha R = 0.05\ln(10)\alpha R_0 e^{-0.05\ln(10)\alpha R}. \tag{A51}$$

Comparing (A51) and (A50), we get the solution

$$\textbf{radar range equation}: R = \frac{W(0.115\alpha R_0)}{0.115\alpha} \ (\text{m}). \tag{A52}$$

References

[1] J. C. Lin, "Noninvasive microwave measurement of respiration," *Proc. IEEE*, vol. 63, no. 10, Oct. 1975, Art. no. 1530.

[2] R. B. Northrop and S. S. Nilakhe, "A no-touch ocular pulse measurement system for the diagnosis of carotid occlusions," *IEEE Trans. Biomed. Eng.*, vol. BME-24, no. 2, pp. 139–148, Mar. 1977.

[3] H. Karsh, "Motion monitor," U.S. Patent 4 122 427, Oct. 1978.

[4] R. B. Northrop, "Ultrasonic respiration/convulsion monitoring apparatus and method for its use," U.S. Patent 4 197 856, Apr. 1980.

[5] G. P. Heldt and R. J. Ward, III, "Evaluation of ultrasound-based sensor to monitor respiratory and nonrespiratory movement and timing in infants," *IEEE Trans. Biomed. Eng.*, vol. 63, no. 3, pp. 619–629, Mar. 2016.

[6] C. Li *et al.*, "A review on recent progress of portable short-range noncontact microwave radar systems," *IEEE Trans. Microw. Theory Techn.*, vol. 65, no. 5, pp. 1692–1706, May 2017.

[7] M. Mercuri *et al.*, "A direct phase-tracking Doppler radar using wavelet independent component analysis for non-contact respiratory and heart rate monitoring," *IEEE Trans. Biomed. Circuits Syst.*, vol. 12, no. 3, pp. 632–643, Jun. 2018.

[8] C. H. Tseng and Y. H. Lin, "24-GHz self-injection-locked vital-sign radar sensor with CMOS injection-locked frequency divider based on push-push oscillator topology," *IEEE Microw. Wireless Compon. Lett.*, vol. 28, no. 11, pp. 1053–1055, Nov. 2018.

[9] F. K. Wang *et al.*, "A novel vital-sign sensor based on a self-injection-locked oscillator," *IEEE Trans. Microw. Theory Tech.*, vol. 58, no. 12, pp. 4112–4120, Dec. 2010.
[10] P. H. Wu, J. K. Jau, C. J. Li, T. S. Horng, and P. Hsu, "Phase- and self-injection-locked radar for detecting vital signs with efficient elimination of DC offsets and null points," *IEEE Trans. Microw. Theory Tech.*, vol. 61, no. 1, pp. 685–695, Jan. 2013.
[11] M. C. Tang, C. Y. Kuo, D. C. Wun, F. K. Wang, and T. S. Horng, "A self- and mutually injection-locked radar system for monitoring vital signs in real time with random body movement cancellation," *IEEE Trans. Microw. Theory Tech.*, vol. 64, no. 12, pp. 4812–4822, Dec. 2016.
[12] R. Adler, "A study of locking phenomena in oscillators," *Proc. IRE*, vol. 34, no. 6, pp. 351–357, Jun. 1946.
[13] L. J. Paciorek, "Injection locking of oscillators," *Proc. IEEE*, vol. 53, no. 11, pp. 1723–1727, Nov. 1965.
[14] B. Razavi, "A study of injection locking and pulling in oscillators," *IEEE J. Solid-State Circuits*, vol. 39, no. 9, pp. 1415–1424, Sep. 2004.
[15] H. C. Chang, "Stability analysis of self-injection-locked oscillators," *IEEE Trans. Microw. Theory Techn.*, vol. 51, no. 9, pp. 1989–1993, Sep. 2003.
[16] W. Pan, J. Wang, J. Huangfu, C. Li, and L. Ran, "Null point elimination using RF phase shifter in continuous-wave Doppler radar system," *Electron. Lett.*, vol. 47, no. 21, pp. 1196–1198, Oct. 2011.
[17] A. Zielinski and Y. Shi, "Quadrature phase detection in an acoustic positioning system," *J. Hydroacoust.*, vol. 9, pp. 227–238, 2006.
[18] B. K. Park, O. Boric-Lubecke, and V. M. Lubecke, "Arctangent demodulation with DC offset compensation in quadrature Doppler radar receiver systems," *IEEE Trans. Microw. Theory Tech.*, vol. 55, no. 5, pp. 1073–1079, May 2007.
[19] C. Li and J. Lin, "Random body movement cancellation in Doppler radar vital sign detection," *IEEE Trans. Microw. Theory Techn.*, vol. 56, no. 12, pp. 3143–3152, Dec. 2008.
[20] F. K. Wang, S. C. Su, M. C. Tang, and T. S. Horng, "Displacement monitoring system based on a quadrature self-injection-locked radar technology," in *Proc. IEEE MTT-S Int. Microw. Symp.*, Jun. 2017, pp. 1363–1366.
[21] J. Wang, X. Wang, L. Chen, J. Huangfu, C. Li, and L. Ran, "Non-contact distance and amplitude independent vibration measurement based on an extended DACM algorithm," *IEEE Trans. Instrum. Meas.*, vol. 63, no. 1, pp. 145–153, Jan. 2014.
[22] C. Gu *et al.*, "Noncontact large-scale displacement tracking: Doppler radar for water level gauging," *IEEE Microw. Wireless Compon. Lett.*, vol. 24, pp. 899–901, Dec. 2014.
[23] H. Gheidi and A. Banai, "An ultra-broadband direct demodulator for microwave FM receivers," *IEEE Trans. Microw. Theory Techn.*, vol. 59, no. 8, pp. 2131–2139, Aug. 2011.
[24] J. Fiser, P. Zitek, and J. Cerveny, "Relay feedback oscillator design for modeling circadian rhythms in cyanobacteria," in *Proc. Int. Mech. Eng. Congr. Expo.*, Denver, CO, USA, 2011, pp. 549–556.
[25] S. H. Yu and P. H. Wu, "Two kinds of self-oscillating circuits mechanically demonstrated," *Int. J. Electron. Commun. Eng.*, vol. 8, no. 7, pp. 1334–1338, 2014.
[26] D. Chen and D. E. Seborg, "PI/PID controller design based on direct synthesis and disturbance rejection," *Ind. Eng. Chem. Res.*, vol. 41, pp. 4807–4822, 2002.
[27] L. Sun, D. Li, and K. Y. Lee, "Optimal disturbance rejection for PI controller with constraints on relative delay margin," *ISA Trans.*, vol. 63, pp. 103–111, 2016.
[28] G. F. Franklin, J. D. Powell, and A. Emami-Naeini, *Feedback Control of Dynamic Systems*, 6th ed. London, U.K.: Pearson, 2010, p. 584.
[29] L. B. Evans and H. E. Bass, "Tables of absorption and velocity of sound in still air at 68° F," Wyle Laboratories, Torrance, CA, USA, Rep. WR 72-2, Jan. 1972.
[30] K. Coffman, *Real World FPGA Design With Verilog*. Englewood Cliffs, NJ, USA: Prentice-Hall, 2000.
[31] M. Rossi, *Acoustics and Electroacoustics*, translated by P. R. W. Roe, Ed. Norwood, MA, USA: Artech House, 1988.
[32] O. Sonbul and A. Kalashnikov, "Determining the operating distance of air ultrasound range finders: Calculations and experiments," *Int. J. Comput.*, vol. 13, no. 2, pp. 125–131, 2014.
[33] T. C. Scott, R. B. Mann, L. Martinez, and E. Roberto, "General relativity and quantum mechanics: towards a generalization of the Lambert W function," *Applicable Algebra Eng., Commun. Comput.*, vol. 17, no. 1, pp. 41–47, 2006.
[34] J. T. Bushberg, J. A. Seibert, E. M. Leidholdt, and J. M. Boone, *The Essential Physics of Medical Imaging*. Philadelphia, PA, USA: Lippincott Williams & Wilkins, 2002, ch. 16.

Shiang-Hwua Yu (M'02) received the M.S. and Ph.D. degrees in control engineering from National Chiao Tung University, Hsinchu, Taiwan, in 1995 and 2001, respectively. In 2004, he joined the faculty of National Sun Yat-sen University, Kaohsiung, Taiwan, where he is currently an Associate Professor of electrical engineering. His research focuses on relay feedback oscillation and its applications on control, detection, and modulation.

Tzyy-Sheng Horng (S'88–M'92–SM'05–F'16) was born in Taichung, Taiwan. He received the B.S.E.E. degree from National Taiwan University, Taipei, Taiwan, in 1985, and the M.S.E.E. and Ph.D. degrees from the University of California, Los Angeles, CA, USA, in 1990 and 1992, respectively. Since 1992, he has been with the Department of Electrical Engineering, National Sun Yat-sen University, Kaohsiung, Taiwan, where he was the Director of the Telecommunication Research and Development Center from 2003 to 2008, the Director of the Institute of Communications Engineering from 2004 to 2007, and is currently a Chair Professor. His current research interests include RF and microwave ICs and components, RF signal integrity for wireless system-in-package, digitally assisted RF technologies, and green radios for cognitive sensors and Doppler radars. He has authored or coauthored more than 250 technical publications in refereed journal and conference proceedings, mostly in IEEE publications. He holds more than 50 patents. He is a member of the IEEE MTT-S Technical Committee MTT-10. He was the recipient of the 1996 Young Scientist Award from the International Union of Radio Science, the 1998 Industry–Education Cooperation Award from the Ministry of Education, Taiwan, the 2011 Chair Professorship awarded by Advanced Semiconductor Engineering, Inc., the 2012 Outstanding Research Award from National Sun Yat-Sen University, and the 2015 and 2018 Outstanding Research Awards from the Ministry of Science and Technology, Taiwan. He has served on the technical program committees of several international conferences including the International Association of Science and Technology for Development, the International Conference on Wireless and Optical Communications, the IEEE Region 10 International Technical Conference, the IEEE International Workshop on Electrical Design of Advanced Packaging and Systems, the Asia–Pacific Microwave Conference, the IEEE Radio and Wireless Symposium, and the Electronic Components and Technology Conference. He was on the Project Review Board of the Programs of Communications Engineering and Microelectronics Engineering at the Ministry of Science and Technology, Taiwan. He was the Founder Chair of the IEEE MTT-S Tainan Chapter in 2009 and an Associate Editor for the IEEE TRANSACTIONS ON MICROWAVE THEORY AND TECHNIQUES from 2012 to 2015.